ADVANCED FUNCTIONAL MATERIALS
www.afm-journal.de

Broad Range Tuning of Phase Transition Property in VO_2 Through Metal-Ceramic Nanocomposite Design

*Jie Jian, Xuejing Wang, Shikhar Misra, Xing Sun, Zhimin Qi, Xingyao Gao, Jianing Sun, Andrea Donohue, Daw Gen Lin, Vilas Pol, Jeffrey Youngblood, Han Wang, Leigang Li, Jijie Huang, and Haiyan Wang**

Vanadium dioxide (VO_2) is a well-studied Mott-insulator because of the very abrupt physical property switching during its semiconductor-to-metal transition (SMT) around 341 K (68 °C). In this work, through novel oxide-metal nanocomposite designs (i.e., Au:VO_2 and Pt:VO_2), a very broad range of SMT temperature tuning from ≈323.5 to ≈366.7 K has been achieved by varying the metallic secondary phase in the nanocomposites (i.e., Au:VO_2 and Pt:VO_2 thin films, respectively). More surprisingly, the SMT T_c can be further lowered to ≈301.8 K (near room temperature) by reducing the Au particle size from 11.7 to 1.7 nm. All the VO_2 nanocomposite thin films maintain superior phase transition performance, i.e., large transition amplitude, very sharp transition, and narrow width of thermal hysteresis. Correspondingly, a twofold variation of the complex dielectric function has been demonstrated in these metal-VO_2 nanocomposites. The wide range physical property tuning is attributed to the band structure reconstruction at the metal-VO_2 phase boundaries. This demonstration paved a novel approach for tuning the phase transition property of Mott-insulating materials to near room temperature transition, which is important for sensors, electrical switches, smart windows, and actuators.

1. Introduction

Over the past several decades, metal-oxide phase transition materials have attracted extensive research interests owing to their dramatic physical property changes during phase transition processes.[1–4] Various phase transition mechanisms have been proposed to explain the transition processes of different materials.[5–8] Meanwhile, tuning of different phase transition properties, such as the transition temperature, transition amplitude, etc., have been achieved using various tuning approaches such as doping, strain tuning, and stoichiometry tuning for varied applications.[9–11]

As one of the phase transition mechanisms, Mott transition describes the phase transitions of a large group of materials named Mott-insulating materials, in which the strong coulomb repulsion between outer orbits electrons plays a critical role.[5] The Mott transition process requires electrons to gain enough energy to overcome the coulomb potential barrier, which can be realized via temperature change or applying stress.[12] Much research has been applied to tune the Mott transition properties, among which strain tuning and doping are two of the common ones. The strain tuning changes the lattice parameters of the materials by building an internal stress, which can significantly change the coulomb repulsion state between electrons and thus reconstruct the energy band structure.[13,14] However, it is difficult to introduce large stress in oxide materials and it can be accompanied with fractures and other defects.[15] By introducing different dopants into the materials, different energy states can be induced into the original energy band structure.[16,17] The tuning amplitude can be controlled by varying the doping level. However, the increase of doping level is generally accompanied with a fast degradation of phase transition induced physical properties change.

Here, we propose a novel approach for Mott transition tuning based on the energy band structure reconstruction around metal/oxide joint contacts. More specifically, here we introduce nanoscale Au and Pt phases into Vanadium dioxide (VO_2) matrix and control the metal phase dimension to achieve effective tuning of VO_2 phase transition properties. By forming metal-ceramic nanocomposite structures, the contact between phase transition oxides and a metallic phase forms a Schottky junction, thereby, bends the energy bands in the oxides, and thus, can achieve tuning of the phase transition properties. In this paper, VO_2, a Mott-insulating material, is selected to demonstrate the novel approach of phase transition tuning. Owing to its fascinating characteristics, e.g., ultrafast

Dr. J. Jian, X. Wang, S. Misra, X. Sun, Z. Qi, X. Gao, Dr. D. G. Lin, Prof. V. Pol, Prof. J. Youngblood, H. Wang, Dr. L. Li, Dr. J. Huang, Prof. H. Wang
School of Materials Engineering
Purdue University
West Lafayette, IN 47907-2045, USA
E-mail: hwang00@purdue.edu
J. Sun, A. Donohue
J. A. Woollam Co. Inc.
Lincoln, NE 68508, USA
Prof. V. Pol
School of Chemical Engineering
Purdue University
West Lafayette, IN 47907-2100, USA
The ORCID identification number(s) for the author(s) of this article can be found under https://doi.org/10.1002/adfm.201903690.

DOI: 10.1002/adfm.201903690

(within 0.1 °C) phase transition from a semiconductor phase to a metallic phase (SMT) at ≈68 °C (341 K),[2,18,19] first-order phase transition from a tetragonal rutile phase to a monoclinic phase,[20] and significant changes in electrical[21–23] and optical properties,[24–26] VO_2 shows great device potential in gas sensors,[27] electrical switches,[28] thermochromic smart windows,[29] thermal actuators,[30] and memory devices, etc. Therefore, the T_c tuning of VO_2 over a broad temperature range is highly desired to meet the different requirements of practical devices.

Very different from the strain effects via various substrates[31–33] and different buffer layers,[34–36] and various doping elements,[37–39] the oxide-metal nanocomposite approach effectively and broadly tunes the phase transition properties while maintaining high crystalline quality of the films. The effecitve tuning of optical properties of VO_2 was also explored.

2. Results and Discussions

2.1. Phase Transition Tuning of VO_2 via Introducing Metallic Phases

Au:VO_2 and Pt:VO_2 nanocomposite thin films were deposited at 600 °C. The microstructural properties of the nanocomposite thin films were characterized by X-ray diffraction (XRD) and transmission electron microscopy (TEM). **Figure 1**a shows the θ–2θ spectra of Au:VO_2 and Pt:VO_2 thin films. Both films show only one VO_2 peak corresponding to (020), indicating highly textured growth of VO_2 along *b*-axis in both films. In Figure S1a,b in the Supporting Information, the VO_2 (011) ϕ-scan of Au:VO_2 thin film shows six peaks with a rotation of 60° between each other, while the ϕ-scan of VO_2 (102) shows no obvious peaks. This result further confirms the VO_2 (020) out-of-plane growth, instead of VO_2(002). The Au:VO_2 thin film shows a major peak of Au (111) at around 38.2°, indicating a (111) out-of-plane preferred growth of Au particles inside VO_2 matrix. No obvious Pt peak has been observed in the θ–2θ spectrum of Pt:VO_2, which suggests that the Pt particles are distributed in VO_2 matrix in polycrystalline nature. Compared to the bulk VO_2 (020) peak position (≈39.97°), the VO_2 (020) peak of Au:VO_2 film slightly shifts to a smaller angle. It indicates a larger (020) *d*-spacing and a tensile strain out-of-plane, which could be induced by the lattice misfit between VO_2 and *c*-cut sapphire substrate and the coupling between VO_2 and Au out-of-plane. The VO_2 (020) peak of Pt:VO_2 film is around 40.02°, which is very close to the bulk peak position, suggesting that the film is relaxed because of the random orientation of the Pt phase.

The cross-sectional scanning TEM (STEM) images in Figure 1b1,c1 show that both Au and Pt form nanoparticle structures uniformly distributed in the VO_2 matrix, as illustrated in the schematic drawing in Figure 1d. The average particle sizes are around 11.7 and 4.2 nm for Au:VO_2 and Pt:VO_2, respectively. It is noted that a thin Au or Pt nucleation layer forms near the film/substrate interface for Au:VO_2 and Pt:VO_2, respectively. The energy dispersed X-ray (EDX) mapping in Figure 1b2,c2 confirms that the Au and Pt nanoparticles are uniformly distributed in the matrix with no or very limited interdiffusion between VO_2 and metal phases. In Figure 1b3,c3, the V signal appears in the metal nanoparticle areas, because the metal phases are surrounded by VO_2 through the TEM foil thickness. With the same deposition parameters, the Pt phase forms much smaller nanoparticles than Au, which is possibly because of the higher surface energy of Pt particles and thus minimized surface energy by forming smaller nanoparticles. Meanwhile, the Pt:VO_2 thin film shows a thinner thickness of around 75 nm compared to the Au:VO_2 thin film (≈110 nm), which could be related to the low deposition rate of Pt by pulsed laser deposition (PLD) system.

The preferred formation of nanocomposite structures instead of alloys is mainly contributed to the high thermal stability and high oxidation resistance of Au and Pt.[40] Besides, the PLD gives high kinetic energy to the ad-atoms, which allow the effective diffusion on the substrate.[41] During depositions, the formation energy of separated phases could be lower than that of the alloys, thus the Au (or Pt) ad-atoms will continue to nucleate on Au (or Pt) nucleus instead of the VO_2 matrix. Since the Au and Pt have good oxidation resistance, the formed Au or Pt nanostructures in the film will have minimum or no oxidation.

In order to further investigate the interfacial coupling between Au and VO_2, high-resolution STEM (HR-STEM) studies were conducted around the Au-VO_2 phase boundaries. **Figure 2**b,c are the HR-STEM images took from the top view (plan view) of the thin film. In the two areas with two different Au particles, the VO_2 phase has the same lattice orientation. Both of the Au particles show a hexagonal lattice structure, but with a rotation of around 2°. This is further confirmed by the fast Fourier transform (FFT) images of the Au particle lattice (shown as insets). The cross-sectional view HR-STEM images in Figure 2d also clearly show Au (111) planes along the out-of-plane direction. The Au (111) textured growth is attributed to the lowest packing energy of the (111) plane. Despite of the (111) preferred out-of-plane growth, the Au particles show two major in-plane orientations. The atomic models of these two cases are generated in Figure 2e,f. One of the in-plane lattice matching relationship (the case in Figure 2b) is identified as Au(011)// VO_2(001), as demonstrated in Figure 2e. The other one (the case in Figure 2c) is identified as Au(011)//VO_2(100), as demonstrated in Figure 2f. Since the β of VO_2 lattice is around 122.6°, the Au lattice of these two cases shows a rotation of about 2°. Moreover, when the Au(011) matches with VO_2(001), the Au particles usually show sharp and flat interfaces along the Au(011)/VO_2(001) contacts. The interfaces in other orientations are curved and distorted. When the Au(011) matches with VO_2(100), in contrast, only the Au(011)/VO_2(100) interfaces are generally sharp and flat.

The SMT properties of Au:VO_2 and Pt:VO_2 thin films were characterized by measuring the electrical resistance variation during phase transition. **Figure 3**a shows the normalized electrical resistance, $\rho = R\ (T)/R$ (260 K), of VO_2 thin films with and without metal nanoparticles as a function of temperature. Compared to the resistance transition curve of the pure VO_2 thin film synthesized with the same deposition parameters, the curve of Au:VO_2 obviously shifts to the lower temperature side, indicating a significant decrease of T_c of the overall film. In contrast, the resistance transition curve of Pt:VO_2 significantly shifts to the higher temperature side, indicating a major

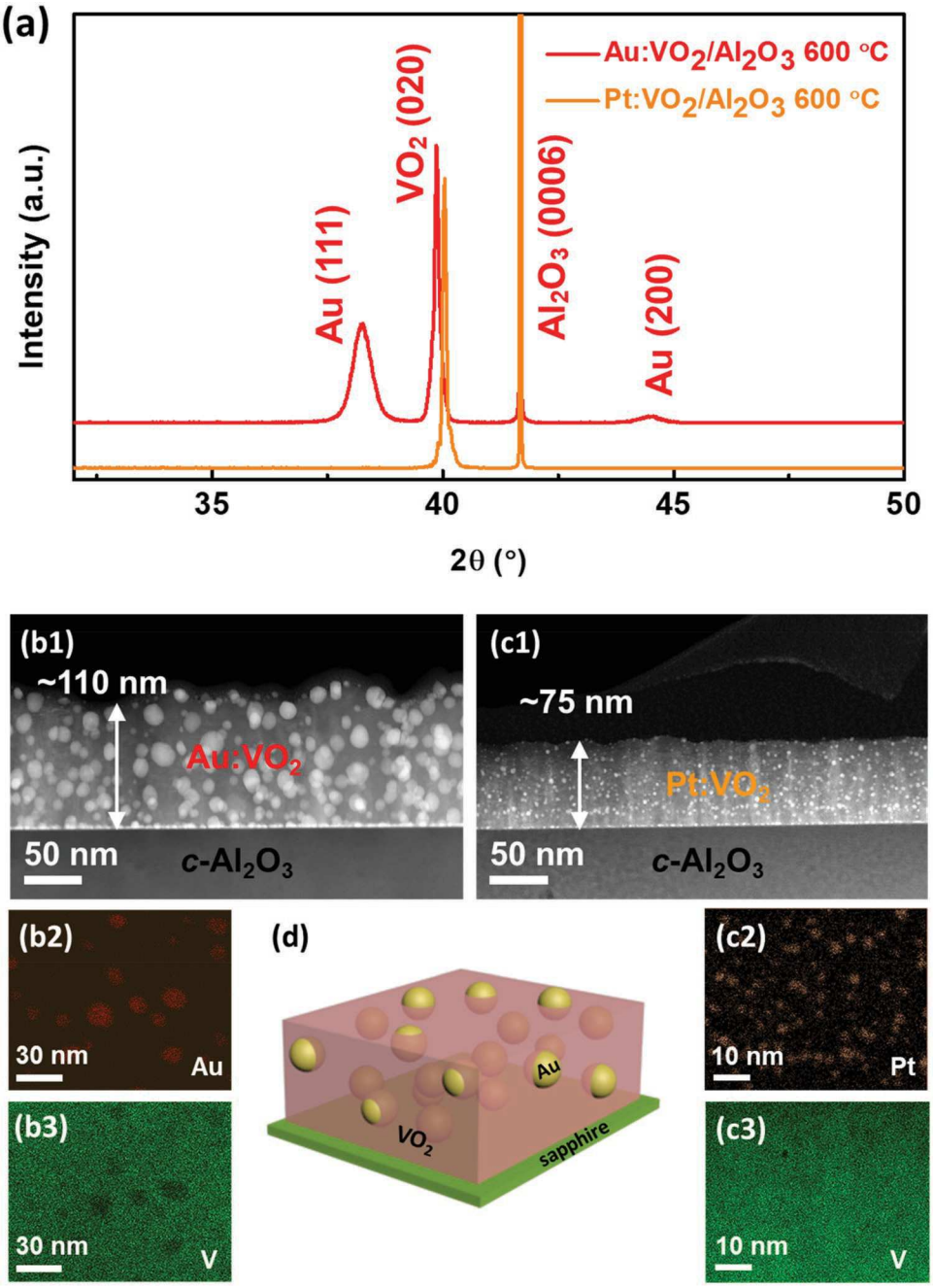

Figure 1. a) XRD θ–2θ spectra of Au:VO_2 and Pt:VO_2 nanocomposite thin films on *c*-cut sapphire substrates. b1) Cross-sectional STEM image of Au:VO_2 thin film. b2,b3) EDX mapping of Au and V elements in the Au:VO_2 thin film. c1) Cross-sectional STEM image of Pt:VO_2 thin film. c2,c3) EDX mapping of Pt and V elements in the Pt:VO_2 thin film. d) Schematic drawing of the 3D microstructure of Au:VO_2 nanocomposite thin film.

increase of T_c. The values of T_c and other SMT parameters, e.g. transition amplitude (ΔA), sharpness (ΔT), and the width of thermal hysteresis (ΔH) were characterized for each film based on the resistance transition curves. As listed in **Table 1**, the T_c of Au:VO_2 is remarkably reduced by 24.5 K to 323.5 K (50.5 °C), while the T_c of Pt:VO_2 increases by 18.7 K to 366.7K (93.7 °C), from the pure VO_2 of 348K (75 °C). Moreover, by introducing metal phases into VO_2 matrix, the overall transition sharpness (ΔT) is decreased by almost 10 K compared to the pure VO_2, indicating much sharper and smoother phase transitions of the metal-VO_2 nanocomposite films. Meanwhile, the ΔA and ΔH are comparable for all three films, suggesting that there is no obvious degradation of the phase transition amplitude and broadening of thermal hysteresis. It is also noted that the pure VO_2 film has a larger resistance value compared to both the Au:VO_2 and Pt:VO_2 thin films deposited at the same temperatures, indicating improved conductivity of the films by introducing metal phases.

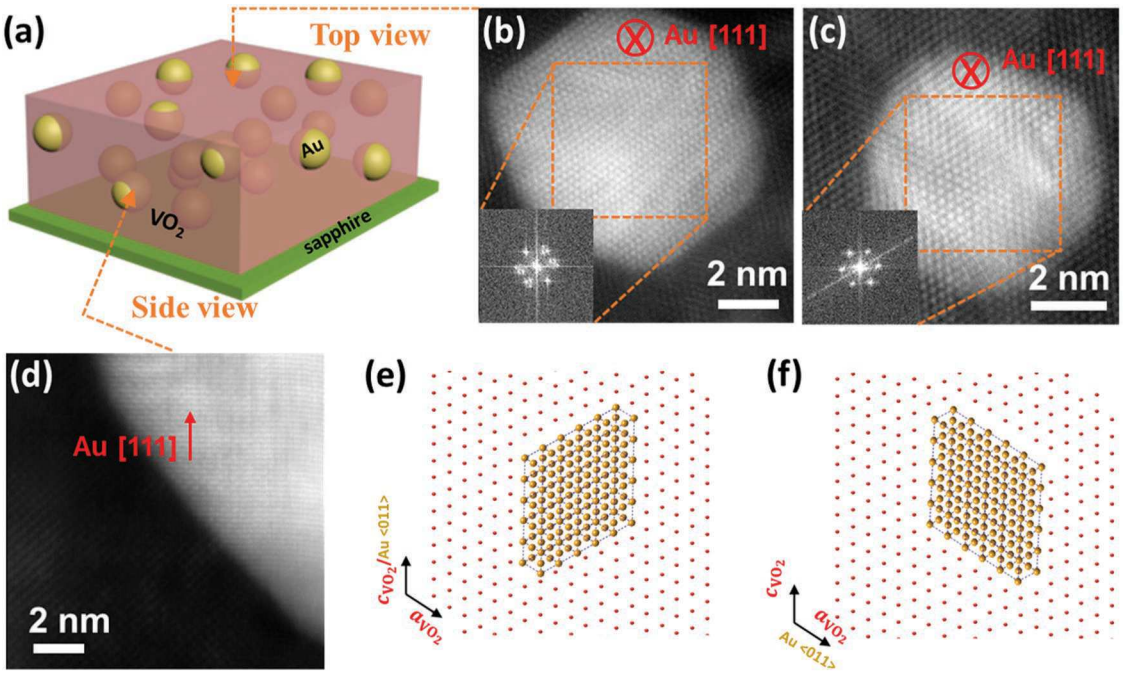

Figure 2. a) Schematic illustration of the view axis of HR-STEM images. b,c) HR-STEM images of the top-view of two Au nanoparticles and the corresponding FFT patterns. The VO_2 matrix shows the same orientation in both images. d) HR-STEM image of the side-view of Au nanoparticle. e) Atomic model of the Au-VO_2 lattice matching relationship, where Au (111) matches with VO_2 (001). f) Atomic model of the other case Au-VO_2 lattice matching, where Au (111) matches with VO_2 (100).

Based on the SMT measurements, it can be concluded that the T_c tunings by introducing metallic phases into VO_2 matrix are comparable or better than many of the prior results using direct metal doping in VO_2.[37,42] Meanwhile, this nanocomposite method maintains excellent film quality, high transition amplitude, and small thermal hysteresis, and thus results in the decrease of transition sharpness.

The T_c tuning of metal-VO_2 nanocomposites is attributed to the concept of energy band structure reconstruction at the metal-VO_2 phase boundaries. Based on the conventional band theories, the VO_2 upper $d\|$ band and the d_π band forms a gap of ≈0.7 eV at room temperature (RT). Considering the coulomb repulsion in Mott model, the electrons will be localized between the V–V pairs by coulomb energy barrier, and thus the upper $d\|$ band will be further lifted up, leaving an actual bandgap larger than 0.7 eV. When the VO_2 is in contact with a metallic phase, they form a Schottky junction and lead to the reconstruction of the energy band structures.[19] As shown in Figure 3b, the work functions (Φ) of pure VO_2 and Au are estimated as 5[43] and 3.7 eV, respectively. The work function of Au nanoparticles is significantly lower than that of bulk Au, usually around 3.3–4 eV.[44] In Figure 3c, when Au and VO_2 form a contact, the Fermi levels of two materials are leveled, which leads to upwards band bending of the conduction band of VO_2. This leaves an electron rich area in the VO_2 side near the phase boundary. Therefore, the electron density of the VO_2 matrix could increase effectively. This can be considered as an effective n-type doping, which will introduce extra energy in the localized electrons in V–V pairs and lower down the coulomb energy barrier (and therefore the bandgap). And because of the lower energy barrier, the temperature required for phase transition will drop down. In contrast, the work function of Pt is around 6 eV,[45] higher than that of VO_2. Thus when they form the Schottky junction, the conduction band of VO_2 will be bent downwards, leaving an electron deficient area in VO_2. The lower electron density in VO_2 leads to higher temperature of the phase transition. In conclusion, the large range T_c tuning of VO_2 can be effectively achieved by selecting the proper metal nanoparticles with either higher or lower work functions of the metal nanoparticles, i.e., smaller work function of the metal than that of VO_2 leads to a decrease of T_c, while a larger work function will cause the increase of T_c. In comparison to the direct doping methods, the nanocomposite approach effectively changes the bandgap and the electron density of VO_2, without introducing unwanted defects and thus maintains its high crystallinity film quality and very sharp phase transition properties (phase transition amplitude and transition width).

2.2. Phase Transition Tuning of VO_2 via Dimension Control of Metallic Phases

More interestingly, the phase transition properties of VO_2 can be further tuned by controlling the Au nanoparticle size in the VO_2 matrix. The Au:VO_2 thin films were deposited at temperatures of 350, 400, and 500 °C to tune the Au particle size. Pure VO_2 thin films were also deposited at these temperatures for comparison. XRD θ–2θ scans were conducted on all the samples and the results were compared with the sample deposited at 600 °C. As shown in **Figure 4**a, all the films have similar θ–2θ spectra, indicating b-axis epitaxial growth of VO_2 matrix and (111) textured growth of Au nanoparticles. The peak

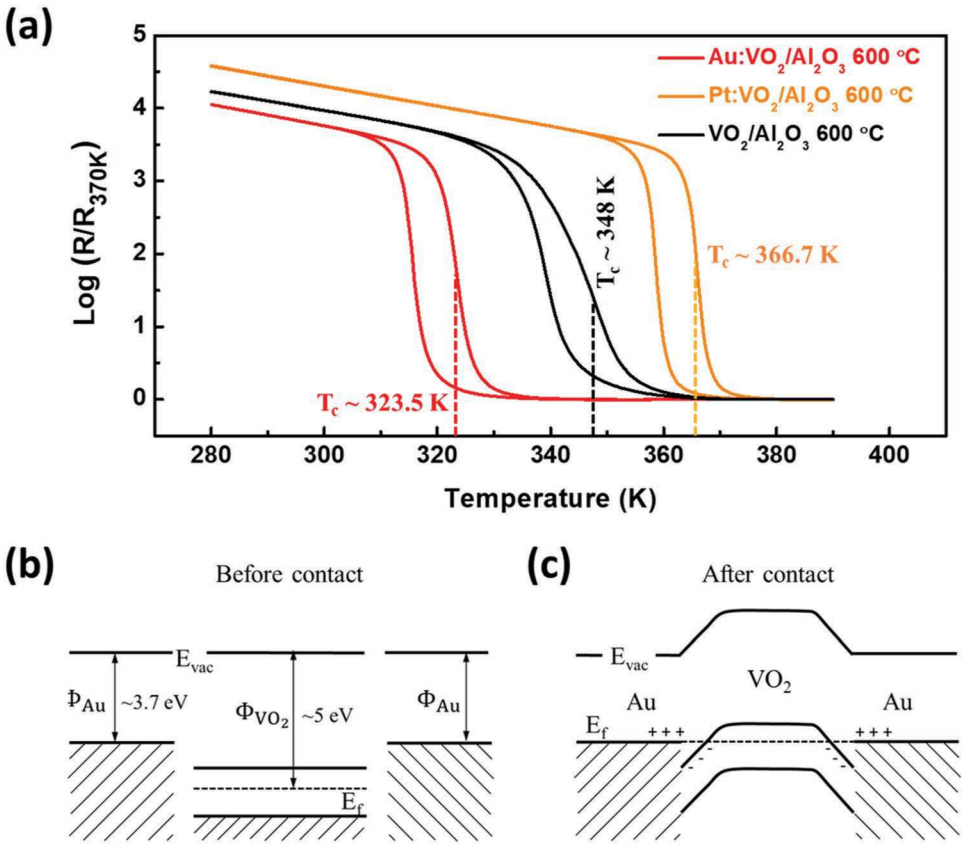

Figure 3. a) Normalized resistance-temperature plots of the Au:VO_2, Pt:VO_2 and pure VO_2 thin films. The T_c of Au:VO_2 shifts downwards while that of Pt:VO_2 shifts upwards compared to the pure VO_2. b) Energy band structure of Au and VO_2 separately. c) Energy band structure of Au and VO_2 when forming contacts. The VO_2 bands are distorted to maintain equal Fermi level.

intensities gradually decrease with the decrease of deposition temperature, suggesting slightly lower film texturing qualities at lower deposition temperatures. The ϕ-scans of Au:VO_2 thin film deposited at 400 °C (see Figure S1c,d, Supporting Information) further confirm that there is no change of film growth orientation at different temperatures. Figure 4b shows the enlarged view of the Au (111) peaks. There is no obvious peak shift of Au for all the samples, while the peak positions of VO_2 (020), shown in Figure 4c, gradually shift towards the bulk VO_2 (020) peak position with the decrease of deposition temperature. It indicates that the substrate induced strain in the VO_2 thin films are gradually relaxed with the decrease of deposition temperature because of the reduced texturing quality of the VO_2 films.

The microstructures of all the samples were further characterized by TEM. As shown in **Figure 5**, the Au particle size obviously decreases with the decreasing of deposition temperature. The film thicknesses of all the samples are around 110 nm, comparable with the Au:VO_2 thin film deposited at 600 °C. The EDX mapping in Figure 5b–d shows that even for the sample with smallest Au particle size (deposited at 350 °C), there is no obvious inter-diffusion between Au and VO_2. Based on the statistic characterizations (see Figure S2, Supporting Information), the average Au particle sizes are determined as 1.7, 4.6, 7.5, and 11.7 nm for the deposition temperatures of 350, 400, 500, and 600 °C, respectively, as plotted in Figure 5g.

The SMT properties of all the Au:VO_2 thin films were characterized and plotted in **Figure 6**a compared with the pure VO_2 thin film deposited at 350 °C. The SMT properties of the other pure VO_2 thin films deposited under different temperatures were plotted in Figure S3 in the Supporting Information. The electrical resistance transition curves show obvious left shift towards lower temperature with the decrease of Au particle size, indicating a further downward tuning of T_c by decreasing Au dimensions. The values of T_c for all the Au-VO_2 and pure VO_2 thin films under various deposition temperatures were plotted in Figure 6b. It is clear that T_c obviously reduces for all the Au-VO_2 thin films from their pure VO_2 counterparts deposited at the same temperature, while the variation on the T_c of the pure VO_2 thin film is minimal. A record low T_c of 301.8 K is achieved in the Au:VO_2 thin film with the

Table 1. SMT characteristics of VO_2 thin film with different metal phases.

	T_c (K)	ΔA	$\Delta T\uparrow$ (K)	ΔH (K)	R_{260K} ($\times 10^4$ Ω)
Au:VO_2	323.5	22 160	4.2	7.7	6.8
Pt:VO_2	366.7	31 800	3.7	8.2	10.7
Pure VO_2	348.0	33 420	13.3	9.1	12.5

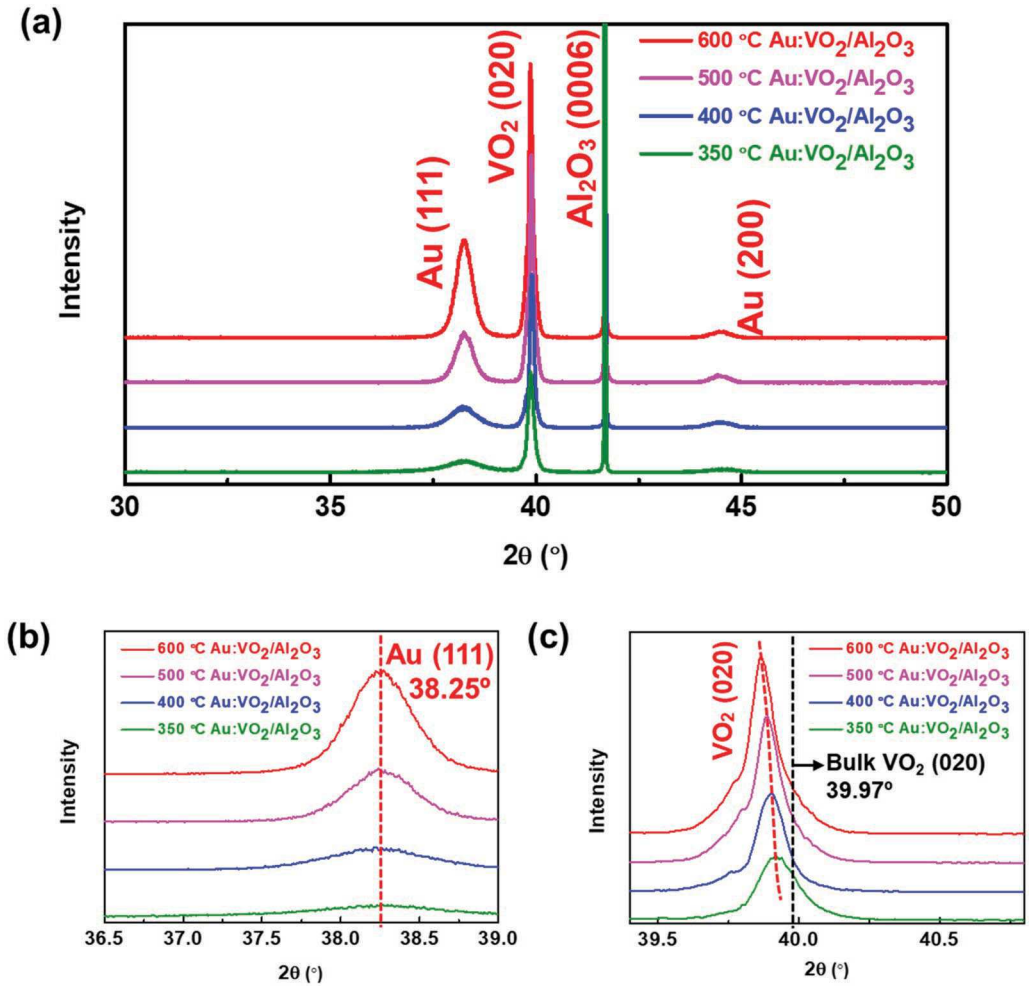

Figure 4. a) XRD θ–2θ spectra of Au:VO_2 nanocomposite thin films deposited at 350, 400, 500, and 600 °C on *c*-cut sapphire substrates. b) Enlarged Au (111) peak area shows no obvious peak shift for all the samples. c) Enlarged VO_2 (020) peak area shows a gradual shift towards the bulk (020) position with the decrease of deposition temperature, indicating gradual relaxation of internal stress.

smallest Au particle size of 1.7 nm, which is more than 40 K lower than the corresponding pure VO_2. The phase transition parameters of all the samples are summarized in **Table 2**. It is noted that for pure VO_2 samples, the transition amplitude (ΔA) decreases and the transition width (ΔT) increases with the decrease of deposition temperature, which is due to the reduction of film crystallinity. However, the Au:VO_2 samples show much lower ΔT values for all the samples which again suggests the high film quality compared to the pure VO_2 samples. This again suggests the effectiveness of T_c tuning using the Au-VO_2 nanocomposite approach with very high film quality and improved phase transition properties (i.e., the same transition amplitude (ΔA) and the reduced transition width (ΔT)). This is attributed to the increase of electron density in VO_2 matrix because of the Au nanoparticles as evidenced by the Hall measurements and charge carrier density calculation in Figure 6c. It is clear that as the grain size reduces, the charge carrier density increases drastically from 3.2×10^{18} to 1.57×10^{19}, which is to be discussed in more detail below. Hall mobility also reduces slightly due to the slightly reduced film quality. The charge carrier density variation is further supported by the measured resistance values at 260 K. As shown in Table 2, the resistances of Au:VO_2 thin films decrease with the decrease of deposition temperatures, suggesting an increase of film charge carrier density with the decrease of Au particle size. In contrast, the resistances of pure VO_2 films increases with the decrease of deposition temperature, which could be attributed to the increase of defect density.

The continuous tuning of T_c with decreasing Au particle size is mainly attributed to the Au-VO_2 phase boundary density change. As shown in Figure 6d, with the same amount of Au in VO_2 matrix, the particles with smaller size will have more total interface areas with VO_2. The width of electron rich area (x_n) in VO_2 beside the phase boundary can be derived from Equation (1) below,

$$x_n = \sqrt{\frac{2\varepsilon\left(\Phi_{VO_2} - \Phi_{Au}\right)}{qN_d}} \tag{1}$$

where ε is the dielectric constant of Au, Φ_{VO_2} and Φ_{Au} are the work functions of VO_2 and Au, respectively, q is the electron charge, and N_d is the bulk VO_2 electron density. Based on the

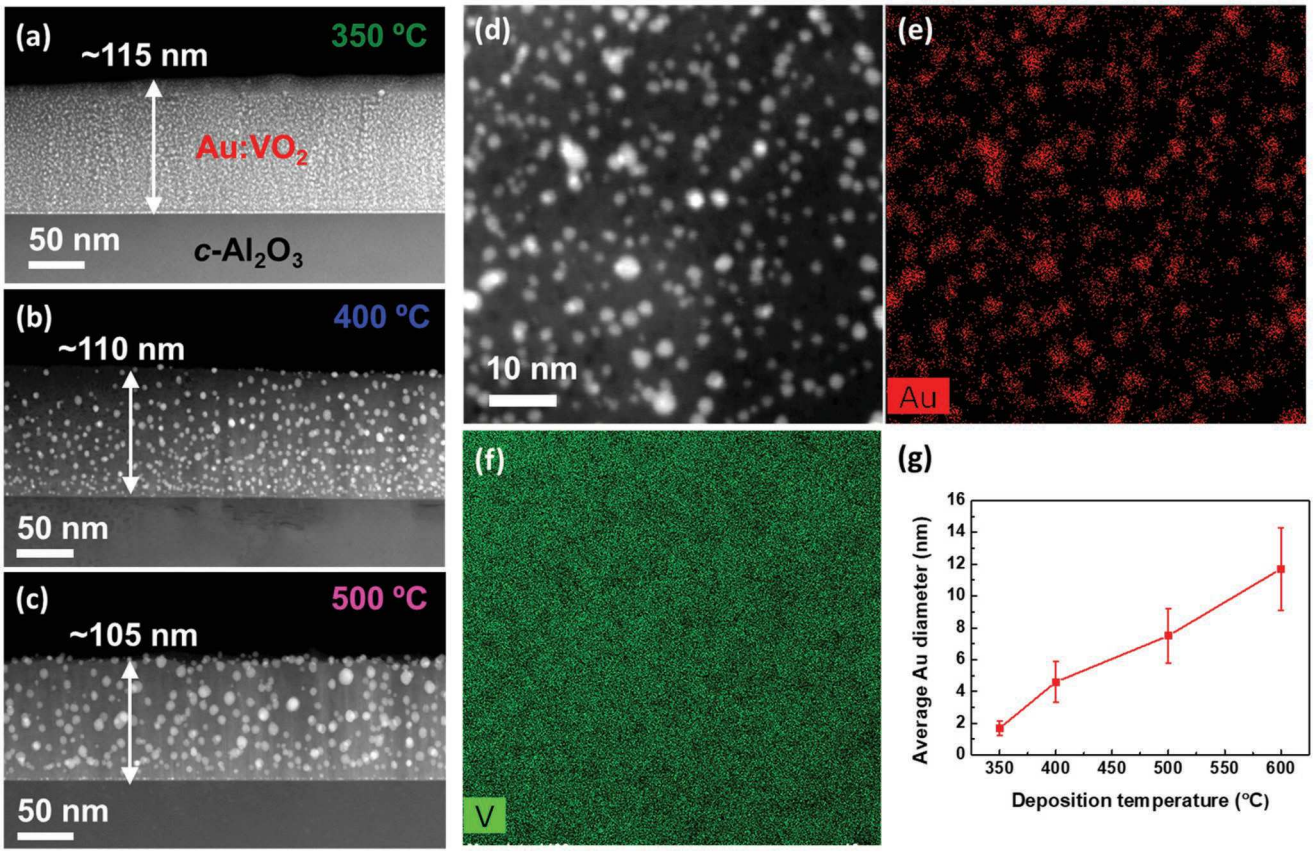

Figure 5. a–c) Cross-sectional STEM images of the Au:VO_2 nanocomposite thin films deposited at 350, 400, and 500 °C, respectively. d) High magnification STEM image of the top view of 350 °C deposited Au:VO_2. e,f) EDX mapping of Au and V elements for the area in (d). g) Plot of the relationship between Au diameter and deposition temperature. Average Au diameter increases with the raise of deposition temperature.

resistance values and the Hall measurement results of pure VO_2 thin films, the N_d of bulk VO_2 decreases with the decrease of deposition temperature. Therefore, x_n will increase with the decrease of Au particle size. The relationship between the total electron rich area ratio (a_{rich}) in VO_2 and the Au particle size can be described in Equation (2),

$$a_{rich} = a\left[\left(1+\frac{2x_n}{d}\right)^3 - 1\right] \quad (2)$$

where a is the Au volume ratio, and d is the Au particle diameter. With the decrease of Au particle size, both the raise of x_n and the drop of d can lead to the increase of a_{rich}. Therefore, the overall electron density in the VO_2 matrix increases, which leads to a continuous drop of T_c.

As the Au phase concentration variation in different Au:VO_2 thin films is another factor that could lead to the T_c change, the Au to V atomic ratios were characterized for all the Au:VO_2 thin films by large-scale EDX quantifications in scanning electron microscopy (SEM). As shown in Figure S4 in the Supporting Information, an area of around 0.5 mm x 0.5 mm has been characterized for each film. The Au to V atomic ratios for the thin films deposited at different temperatures are very similar, around 12.8% (±1%). Raman spectrum characterizations were further conducted on all the nanocomposite thin films to identify the deposition temperature impacts on the VO_2 stoichiometry. Figure S5 in the Supporting Information shows the Raman spectra of Au:VO_2 deposited at 350 and 600 °C, and the pure VO_2 deposited at 600 °C. All three spectra are very comparable, with no obvious peak shift. It indicates that the samples are with similar stoichiometry. Furthermore, the Raman signal intensity increase with the decrease of Au particle size. It suggests that the Au particles have surface plasmon enhancement effects, which strengthens with the decrease of Au nanoparticle size. Based on the above observations, it can be concluded that the T_c tuning of Au:VO_2 thin films by Au particle size variation is mainly attributed to the increase of Au-VO_2 phase boundary density and the significantly enhanced charge carrier density in the Au-VO_2 thin films.

Figure 7a presents the UV–vis–near-infrared (NIR) transmittance spectra of the Au:VO_2 thin films grown at four different temperatures. The inset shows the corresponding Tauc plots. The optical transmittance spectra and the corresponding Tauc plots for pure VO_2 thin films deposited at different temperatures are presented in Figure S6a,b in the Supporting Information. The absorption edge of Au:VO_2 films shows clear red-shifts upon incorporation of Au nanoparticles for all case. A detailed bandgap calculation of the nanocomposite films is plot in Figure 7b.[46,47] The pure VO_2 bandgap shows a monotonic increase from 1.79 eV (grown at 600 °C) to 2.33 eV (grown at

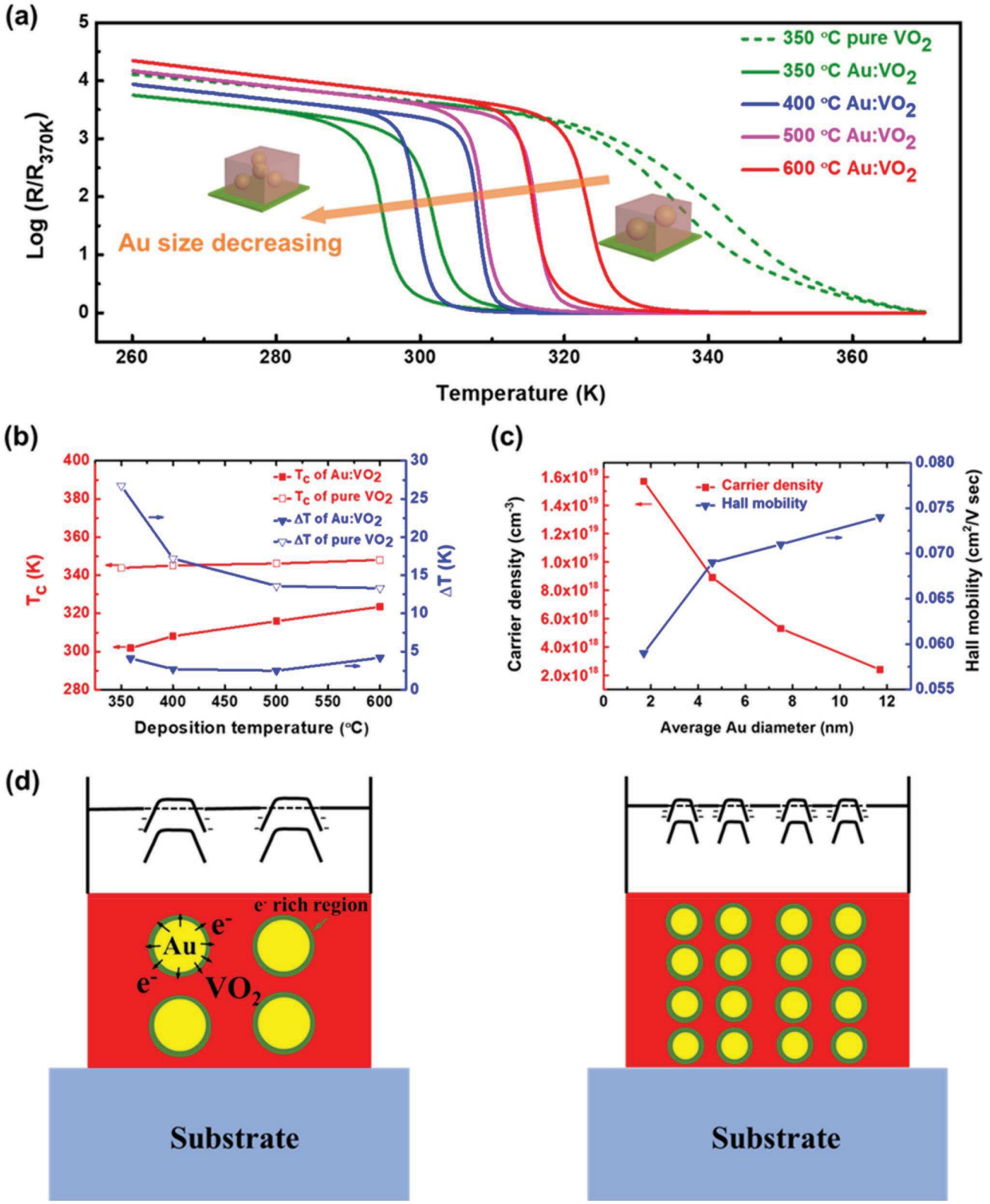

Figure 6. a) Normalized resistance-temperature plots of the Au:VO_2 thin films deposited at 350, 400, 500, and 600 °C and the pure VO_2 thin film deposited at 350 °C. b) The T_c and ΔT plots for both Au:VO_2 and pure VO_2 thin films as a function of deposition temperature. c) The electron carrier density and hall mobility in the Au:VO_2 thin films as a function of the average Au diameter. d) 2D schematic drawing of the Au:VO_2 nanocomposites with the same Au/VO_2 ratio but different Au particle size. The film with smaller Au size contains more volume of electron rich regimes.

Table 2. SMT characteristics of Au:VO_2 and pure VO_2 thin film deposited at different temperatures.

	Deposition temperature (°C)	T_c (K)	ΔA	$\Delta T\uparrow$ (K)	ΔH (K)	R_{260K} ($\times 10^4$ Ω)
Au:VO_2	350	301.8	5640	4.1	7.1	2.7
	400	308.1	8650	2.5	8.7	3.4
	500	315.9	14 700	2.7	7.3	4.9
	600	323.5	22 160	4.2	7.7	6.8
Pure VO_2	350	343.8	12 900	26.7	8.3	18.1
	400	345.1	18 100	17.2	8.3	17.4
	500	346.2	22 900	13.6	7.2	14.6
	600	348.0	31 800	13.3	9.1	12.5

350 °C) as the deposition temperature decreases, which is due to the increase of disorders and defects density in the samples under lower growth temperature. Interestingly, incorporation of Au nanoparticles in VO_2 matrix further decreases its bandgap by 0.07–0.19 eV as compared to the pure VO_2 cases. Such E_g reduction further confirms the Au particle induced energy band structure reconstruction as illustrated in Figure 3b. Additionally, all Au:VO_2 nanocomposite films present an obvious plasmonic absorption peak position shift systematically as shown in Figure 7b. Such large shift in the plasmonic absorption peak from 609 nm (grown at 350 °C) to 687 nm (grown at 600 °C) is believed to be due to increase in Au nanoparticle size ≈1.7 nm (grown at 350 °C) to ≈11.7 nm (grown at 600 °C).

Tunability of the dielectric response of Au:VO_2 nanocomposite films was evaluated using angular dependent spectroscopic ellipsometry measurement and the fitted results of dielectric permittivity ε' (real part) for RT (300 K) (semiconductor before phase transition) and at 80 °C (metallic after phase transition) are presented in Figure 7c,d. The results of dielectric permittivity ε'' (imaginary part) are presented

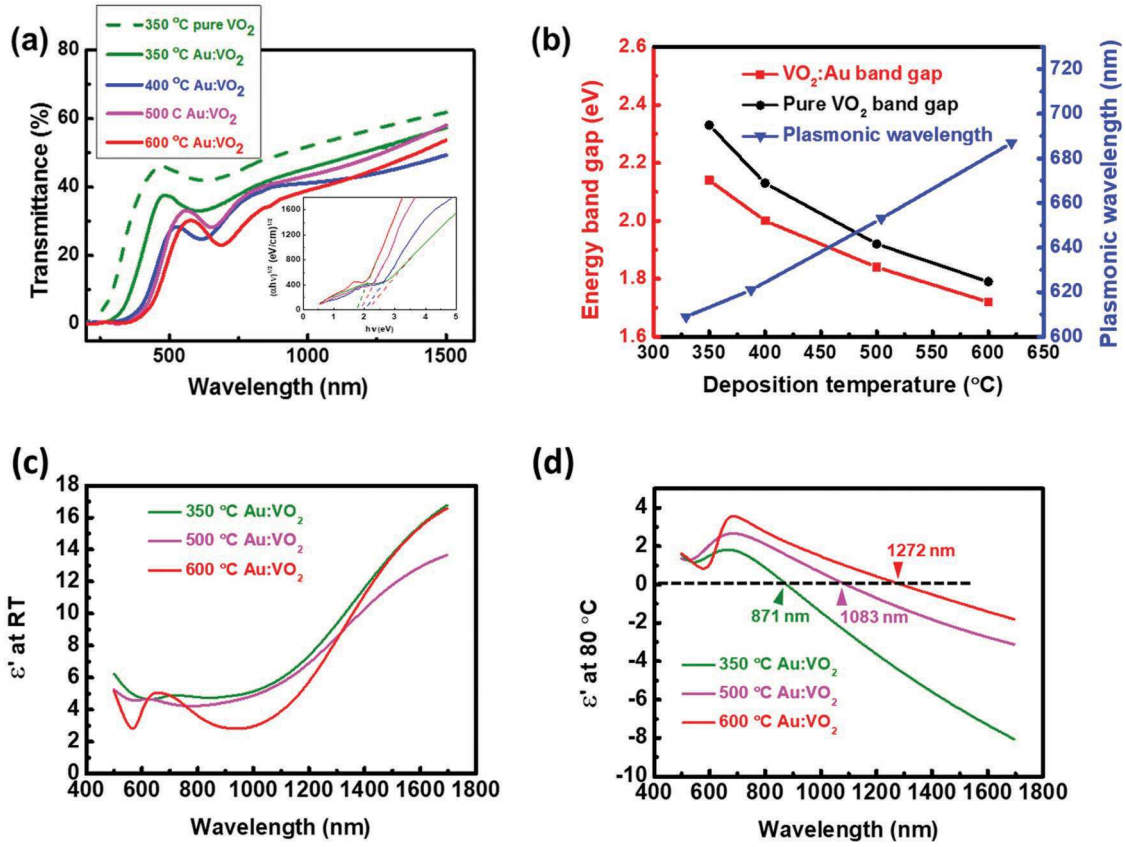

Figure 7. a) Optical transmittance of the Au:VO_2 thin films deposited at 350, 400, 500, and 600 °C and the pure VO_2 thin film deposited at 350 °C. The inset is the Tauc plots for all the Au:VO_2 films. b) The energy bandgap of Au:VO_2 and pure VO_2 thin films with different deposition temperature. And the plot of plasmonic resonance wavelength versus deposition temperature. c) The dielectric permittivity ε' (real part) at RT and d) at 80 °C for Au:VO_2 thin films deposited 350, 500, and 600 °C.

in Figure S6c,d, in the Supporting Information. The ellipsometer parameters ψ and Δ were fitted assuming isotropic response ($\varepsilon[001] = \varepsilon[010] = \varepsilon[100]$), with the use of general oscillator models to make it Kramers–Kronig consistent (see Methods section). The ε' of Au-VO_2 films at RT shows the normal dispersion curve with the plasmonic absorption of Au in the 600–700 nm regime. The ε' is positive throughout the entire wavelength regime, consistent with the observed semiconducting behaviors of the films at 300 K. The ε' values decrease with the decrease of the Au particle size (except for the plasmonic absorption wavelength regimes), indicating an increase of the overall electron density, consistent with the Hall measurement results. In contrast, at 80 °C, all the Au:VO_2 nanocomposite films undergo SMT evident by the negative ε' at wavelengths >1100 nm. More interestingly, the epsilon-near zero (ENZ) wavelength can be tuned by varying Au particles size, i.e., as the Au nanoparticle size reduces (deposition temperature reduces), the ENZ wavelength reduces. Therefore, Au particles size plays a significant role in tuning the overall permittivity and the ENZ wavelength.

Overall, all the electrical phase transition property measurements and optical property tuning data suggest the obvious phase transition property tuning demonstrated by metal-VO_2 nanocomposite design approach. The major observations include: 1) different metal with different work function effectively tune the transition properties by charge carrier injection or depletion; more specifically, the Au with a smaller work function injects charge carriers into VO_2 and tunes the T_c downwards, while the Pt with a larger work function depletes charge carriers from VO_2 and tunes the T_c upwards, 2) metal nanoparticle size also effectively tunes the phase transition properties, i.e., T_c is tuned from 323.5 to 301.8 K when the Au particle sizes decreases from 11.7 to 1.7 nm, and 3) high film quality and phase transition properties still remain. Compared with prior metallic ion doping approach, a major advantage of this nanocomposite approach is that it maintains its excellent epitaxial quality, high transition amplitude, and narrow transition sharpness of VO_2. These results are supported by other related research works.[48–50] For example, Xu et al. has reported that the VO_2 thin films with Au particles covered on top showed a T_c of around 50 °C.[49] Most recently, Fu et al. proposed that the Au particles can tune the bandwidth in VO_2, which gives a support on our hypothesis.[51]

Combining the metal selection and particle size tuning, the record low T_c of 301.8 K achieved by this metal-VO_2 nanocomposite design approach demonstrates the feasibility of broad range phase transition property tuning towards RT applications of phase change materials for temperature sensors, resistive switches, thermal actuators, tunable smart window, etc. For example, the tunable smart window is usually designed to tune the light intensity transmitted into a room at different temperatures, which commonly works around RT. With the novel approach, the T_c of VO_2 can be tuned to the working temperature range of smart window. Moreover, the novel approach maintains high light transmittance of the material comparable to pure VO_2 at low temperatures. And the sharp transition width can provide fast temperature response for the window. Therefore, the VO_2 nanocomposites can be an ideal candidate for the tunable smart window.

3. Conclusions

In summary, we have demonstrated a new concept of interface band structure reconstruction for effective phase transition property tuning in VO_2 thin films by introducing metal nanoparticles into VO_2 matrix. Both Au:VO_2 and Pt:VO_2 nanocomposite thin films have been achieved with the metal phases forming uniformly distributed nanoparticles inside the VO_2 matrix. The T_c has been reduced to 323.5 K (Au:VO_2) and increased to 366.7 K (Pt:VO_2) from 348 K for the pure VO_2 case. This result clearly demonstrates that selecting different metals with different work function leads to the band structure reconstruction at the interfaces, i.e., metals with higher work function than VO_2 lead to higher charge carrier density in VO_2 and lower T_c, while metals with lower work functions lead to charge carrier depletion from VO_2 matrix and thus a higher T_c. A record low T_c value of 301.8 K (28.8 °C, near RT) by further reducing the Au particle size to ≈1.7 nm has been demonstrated because of the increased phase boundary density with the decrease of particles. The optical properties, such as plasmonic absorption frequency, complex dielectric function, and ENZ wavelength, were also effectively tuned by introducing metal phases. Furthermore, this approach can be adopted in other Mott-insulating oxides towards effective phase change property tuning and thus paves a powerful tuning approach towards the practical applications of Mott-insulating materials in electronic- and optical-based devices.

4. Experimental Section

All the VO_2-Au and VO_2-Pt nanocomposite thin films were deposited by a PLD system with a KrF excimer laser (Lambda Physik Compex Pro 205, $\lambda = 248$ nm). The laser beam was focused to obtain an energy density of approximately 3 J cm^{-2} at a 45° angle of incidence. The pure VO_2 thin films were deposited using a V_2O_5 target hot pressed and sintered at 600 °C. The Au:VO_2 and Pt:VO_2 thin films were deposited by attaching an Au or Pt foil piece on top of the pure V_2O_5 target. All the thin films were deposited at the oxygen pressure of 10 mtorr and the laser frequency of 2 Hz. The Au:VO_2 and Pt:VO_2 thin film was deposited at the substrate temperature of 600 °C for 4000 pulses. The Au dimensions were then controlled by changing the substrate temperatures to 350, 400, and 500 °C. In order to maintain similar Au phase concentrations for the Au:VO_2 thin films deposited at different temperatures, the laser spots were carefully aligned to hit on a similar position on the target. The deposition durations were optimized to achieve similar thicknesses as the 600 °C deposited Au:VO_2.

The microstructures of the as-deposited films were characterized by XRD and TEM. XRD θ–2θ scans and ϕ-scans were performed using a PANalytical Empyrean 2 X-ray diffractometer with Cu K_α radiation. High angle annual dark field scanning TEM images were acquired by Thermo Scientific Talos F200X analytical microscope with a point-to-point resolution of 0.16 nm. TEM samples were prepared using a standard cross-section sample preparation procedure, including manual grinding, polishing, dimpling, and a final ion milling step (PIPS 691 precision ion polishing system, 3.7 keV). The electrical resistivity transition of all the samples were measured with temperature varied from 260 to 390 K in a physical property measurement system (PPMS, Quantum Design). The Hall measurements were conducted with the magnetic field scanning from −1 to 1 Tesla in the PPMS. The metal phase concentrations in the nanocomposite thin films were characterized by the EDX tool in a Quanta 600 SEM. The stoichiometry of the thin films were characterized using a homemade Raman spectrometer.

The optical transmittance characterizations were carried using a UV–vis–NIR absorption spectrophotometer (PerkinElmer Lambda 1050). The permittivity of the Au:VO_2 nanocomposite thin films was evaluated using spectroscopic ellipsometry (JA Woollam RC2). The incident angle was varied from 55° to 75°, with a step size of 10°. The ellipsometer parameters ψ and Δ are related by the equation: $r_p/r_s = \tan(\psi)\, e(i\Delta)$, where r_p and r_s are the reflection coefficient for the p-polarization and s-polarization light, respectively. The parameters ψ and Δ were fitted using an appropriate model to calculate the dielectric permittivity. The ψ and Δ are measured at different angles to improve the accuracy of the fitted model. The calculations were carried out using the ellipsometry software CompleteEASE. A general oscillator layer consisting of one Drude oscillator and one Lorentz oscillator (Drude-Lorentz model) was used to fit the metallic Au-VO_2 nanocomposite at 80 °C.

Supporting Information

Supporting Information is available from the Wiley Online Library or from the author.

Acknowledgements

This work was supported by the U.S. National Science Foundation (DMR-1809520). Han W. and H.W. acknowledge the access of high-resolution STEM/TEM supported by the U.S. National Science Foundation (DMR-1565822).

Conflict of Interest

The authors declare no conflict of interest.

Keywords

band structure reconstruction, metal-oxide nanocomposites, Mott-insulator, phase transition property tuning, VO_2

Received: May 8, 2019
Revised: June 16, 2019
Published online: July 5, 2019

[1] A. Urushibara, Y. Moritomo, T. Arima, A. Asamitsu, G. Kido, Y. Tokura, *Phys. Rev. B* **1995**, *51*, 14103.
[2] M. Imada, A. Fujimori, Y. Tokura, *Rev. Mod. Phys.* **1998**, *70*, 1039.
[3] H. Kuwahara, Y. Tomioka, A. Asamitsu, Y. Moritomo, Y. Tokura, *Science* **1995**, *270*, 961.
[4] A. V. Boris, Y. Matiks, E. Benckiser, A. Frano, P. Popovich, V. Hinkov, P. Wochner, M. Castro-Colin, E. Detemple, V. K. Malik, C. Bernhard, T. Prokscha, A. Suter, Z. Salman, E. Morenzoni, G. Cristiani, H. U. Habermeier, B. Keimer, *Science* **2011**, *332*, 937.
[5] R. Jordens, N. Strohmaier, K. Gunther, H. Moritz, T. Esslinger, *Nature* **2008**, *455*, 204.
[6] R. E. Peierls, *More Surprises in Theoretical Physics*, Princeton University Press, Princeton, NJ **1991**.
[7] L. M. Falicov, J. C. Kimball, *Phys. Rev. Lett.* **1969**, *22*, 997.
[8] A. Cavalleri, C. Toth, C. W. Siders, J. A. Squier, F. Raksi, P. Forget, J. C. Kieffer, *Phys Rev Lett.* **2001**, *87*, 237401.
[9] J. Cao, E. Ertekin, V. Srinivasan, W. Fan, S. Huang, H. Zheng, J. W. L. Yim, D. R. Khanal, D. F. Ogletree, J. C. Grossmanan, J. Wu, *Nat. Nanotechnol.* **2009**, *4*, 732.
[10] T. Kimura, Y. Tomioka, R. Kumai, Y. Okimoto, Y. Tokura, *Phys. Rev. Lett.* **1999**, *83*, 3940.
[11] S. X. Zhang, I. S. Kim, L. J. Lauhon, *Nano Lett.* **2011**, *11*, 1443.
[12] M. Cyrot, *J. Phys.* **1972**, *33*, 125.
[13] S. Asanuma, P. H. Xiang, H. Yamada, H. Sato, I. H. Inoue, H. Akoh, A. Sawa, K. Ueno, H. Shimotani, H. Yuan, M. Kawasaki, Y. Iwasa, *Appl. Phys. Lett.* **2010**, *97*, 142110.
[14] S. Mukherjee, N. F. Quackenbush, H. Paik, C. Schlueter, T. L. Lee, D. G. Schlom, L. F. J. Piper, W. C. Lee, *Phys. Rev. B* **2016**, *93*, 241110.
[15] J. Jian, A. P. Chen, Y. X. Chen, X. H. Zhang, H. Y. Wang, *Appl. Phys. Lett.* **2017**, *111*, 153102.
[16] D. B. Mcwhan, A. Menth, J. P. Remeika, W. F. Brinkman, T. M. Rice, *Phys. Rev. B* **1973**, *7*, 1920.
[17] P. A. Lee, N. Nagaosa, X. G. Wen, *Rev. Mod. Phys.* **2006**, *78*, 17.
[18] F. J. Morin, *Phys. Rev. Lett.* **1959**, *3*, 34.
[19] J. B. Goodenough, *J. Solid State Chem.* **1971**, *3*, 490.
[20] V. Eyert, *Ann. Phys.* **2002**, *11*, 650.
[21] A. Zylbersztejn, N. F. Mott, *Phys. Rev. B* **1975**, *11*, 4383.
[22] K. D. Rogers, J. A. Coath, M. C. Lovell, *J. Appl. Phys.* **1991**, *70*, 1412.
[23] G. Stefanovich, A. Pergament, D. Stefanovich, *J. Phys.: Condens. Matter* **2000**, *12*, 8837.
[24] M. Benmoussa, E. Ibnouelghazi, A. Bennouna, E. L. Ameziane, *Thin Solid Films* **1995**, *265*, 22.
[25] E. E. Chain, *Appl. Opt.* **1991**, *30*, 2782.
[26] H. S. Choi, J. S. Ahn, J. H. Jung, T. W. Noh, D. H. Kim, *Phys. Rev. B* **1996**, *54*, 4621.
[27] E. Strelcov, Y. Lilach, A. Kolmakov, *Nano Lett.* **2009**, *9*, 2322.
[28] S. Nori, T. H. Yang, J. Narayan, *J. Miner.* **2011**, *63*, 29.
[29] Z. L. Huang, S. H. Chen, C. H. Lv, Y. Huang, J. J. Lai, *Appl. Phys. Lett.* **2012**, *101*, 191905.
[30] A. Rua, F. E. Fernandez, N. Sepulveda, *J. Appl. Phys.* **2010**, *107*, 074506.
[31] S. Lee, I. N. Ivanov, J. K. Keum, H. N. Lee, *Sci. Rep.-Uk* **2016**, *6*, 19621.
[32] J. Jian, A. P. Chen, W. R. Zhang, H. Y. Wang, *J. Appl. Phys.* **2013**, *114*, 234103.
[33] H. Koo, S. Yoon, O. J. Kwon, K. E. Ko, D. Shin, S. H. Bae, S. H. Chang, C. Park, *J. Mater. Sci.* **2012**, *47*, 6397.
[34] T. W. Chiu, K. Tonooka, N. Kikuchi, *Appl. Surf. Sci.* **2010**, *256*, 6834.
[35] J. Jian, X. J. Wang, L. G. Li, M. Fan, W. R. Zhang, J. J. Huang, Z. M. Qi, H. Y. Wang, *ACS Appl. Mater. Interfaces* **2017**, *9*, 5319.
[36] Y. Muraoka, Z. Hiroi, *Appl. Phys. Lett.* **2002**, *80*, 583.
[37] N. R. Mlyuka, G. A. Niklasson, C. G. Granqvist, *Appl. Phys. Lett.* **2009**, *95*, 171909.
[38] L. Q. Mai, B. Hu, T. Hu, W. Chen, E. D. Gu, *J. Phys. Chem. B* **2006**, *110*, 19083.
[39] M. Soltani, M. Chaker, E. Haddad, R. V. Kruzelecky, J. Margot, *Appl. Phys. Lett.* **2004**, *85*, 1958.
[40] L. Li, L. Sun, J. S. Gomez-Diaz, N. L. Hogan, P. Lu, F. Khatkhatay, W. Zhang, J. Jian, J. Huang, Q. Su, M. Fan, C. Jacob, J. Li, X. Zhang, Q. Jia, M. Sheldon, A. Alu, X. Li, H. Wang, *Nano Lett.* **2016**, *16*, 3936.
[41] X. Wang, J. Jian, S. Diaz-Amaya, C. E. Kumah, P. Lu, J. Huang, D. G. Lim, V. G. Pol, J. P. Youngblood, A. Boltasseva, L. A. Stanciu, D. M. O'Carroll, X. Zhang, H. Wang, *Nanoscale Adv.* **2019**, *1*, 1045.
[42] I. Takahashi, M. Hibino, T. Kudo, *Jpn. J. Appl. Phys.* **2001**, *40*, 1391.
[43] C. Ko, Z. Yang, S. Ramanathan, *ACS Appl. Mater. Interfaces* **2011**, *3*, 3396.
[44] Y. J. Zhang, O. Pluchery, L. Caillard, A. F. Lamic-Humblot, S. Casale, Y. J. Chaba, M. Salmeron, *Nano Lett.* **2015**, *15*, 51.
[45] H. S. Zheng, Y. Zhou, S. Gangopadhyay, *J. Appl. Phys.* **2015**, *117*, 044503.

[46] F. Wooten, *Optical Properties of Solids* (Academic, New York, **1972**).
[47] S. Hu, S. Y. Li, R. Ahuja, C. G. Granqvist, K. Hermansson, G. A. Niklasson, R. H. Scheicher, *Appl. Phys. Lett.* **2012**, *101*, 201902.
[48] M. Maaza, O. Nemraoul, C. Sella, A. C. Beye, *Gold Bull.* **2005**, *38*, 100.
[49] G. Xu, C. M. Huang, M. Tazawa, P. Jin, D. M. Chen, L. Miao, *Appl. Phys. Lett.* **2008**, *93*, 61911.
[50] S. Prayakarao, B. Mendoza, A. Devine, C. Kyaw, R. B. van Dover, V. Liberman, M. A. Noginov, *Appl. Phys. Lett.* **2016**, *109*, 061105.
[51] G. S. Fu, X. K. Ning, M. J. Chen, S. F. Wang, P. Liu, J. L. Wang, X. W. Li, *J. Am. Ceram. Soc.* **2019**, *102*, 2761.